energies

MDPI

Article

Inertia and Frequency Stability Assessment for Renewable-Rich Distribution Feeders

Samuel A. Ibikunle [1,*], Oyeniyi Akeem Alimi [2] and Evans E. Ojo [1]

[1] Department of Electrical Power Engineering, Durban University of Technology, Durban 4001, South Africa; evanso@dut.ac.za
[2] Department of Information Systems, Durban University of Technology, Durban 4001, South Africa; oyeniyia@dut.ac.za
* Correspondence: 22494870@dut4life.ac.za

Abstract

This study evaluates a disturbance-informed, planning-level workflow for assessing steady-state feeder performance and post-disturbance frequency security in renewable-rich distribution networks. The workflow links feeder operation in DIgSILENT PowerFactory to reduced-order frequency-security screening in OpenModelica and PSAT, with Pandapower used as an independent steady-state cross-check. The IEEE 33-bus feeder includes distributed photovoltaic units, DFIG-based wind generation, and a grid-forming battery energy storage system (BESS). Hourly feeder time-series results are used to identify renewable-output deficits, and each deficit is converted from MW to the common 10 MVA dynamic-system base before being applied as a conservative step disturbance. The steady-state validation gives a maximum voltage mismatch of 0.0155 pu, within the adopted 2% screening limit. The cross-tool frequency benchmark shows close agreement for nadir and settling time, while RoCoF is interpreted conservatively because of its sensitivity to numerical differentiation and event implementation. As renewable penetration increases from 0% to 100%, the minimum bus voltage remains close to 1.0 pu (0.9999–0.9991 pu), the maximum bus voltage rises from 1.0295 pu to 1.0826 pu, and feeder losses increase from 0.0246 MW to 0.1531 MW. The 24 h assessment gives a maximum daily voltage of 1.0755 pu at 100% penetration, while loading remains below thermal limits. For the corrected 75% severe event (0.3048 MW; −0.0305 pu on the 10 MVA base), the 2 MW droop-plus-FFR case improves the nadir from 49.9695 Hz without support to 49.9924 Hz. Voltage therefore becomes the earliest binding screening constraint from 50% penetration onward, whereas thermal loading and supported frequency nadir remain non-binding under the studied conditions.

Keywords: battery energy storage system; frequency stability; frequency nadir; grid-forming control; renewable penetration; distribution feeder

Check for updates

Academic Editor: Claus Leth Bak

Received: 5 June 2026
Revised: 5 July 2026
Accepted: 6 July 2026
Published: 20 August 2026

Copyright: © 2026 by the authors. Licensee MDPI, Basel, Switzerland. This article is an open access article distributed under the terms and conditions of the Creative Commons Attribution (CC BY) license.

1. Introduction

High penetrations of converter-interfaced renewable generation can improve feeder voltages by supplying demand closer to the point of consumption; yet, the same operating condition may reduce the effective inertial support seen by the wider power system and increase sensitivity to rapid active-power imbalances [1,2]. Accordingly, renewable-rich feeder planning is no longer purely a steady-state task. In radial distribution systems, planners and operators are expected to assess voltage rise, reverse power flow, and losses

together with the frequency implications of renewable variability and the capability of storage-based support, in order to preserve security and stability margins.

The recent literature provides important context for this stability problem in four related areas. First, hosting-capacity and feeder-planning studies emphasize voltage rise, reverse power flow, and loss behaviour in active distribution systems [3,4]. These studies are valuable for steady-state planning, but they usually stop at feeder operating indices and do not translate operating-point changes into post-disturbance frequency-security assessment. Second, low-inertia frequency-planning studies show that declining synchronous support worsens RoCoF and nadir margins as renewable penetration rises [5–7]; however, these studies are often system-level and are not always anchored to a specific feeder operating state. Third, grid-forming, synthetic-inertia, and fast-frequency-response studies examine how converter-based support can improve disturbance arrest [8–12], but many of them assume externally imposed disturbance profiles rather than renewable-deficit events extracted from feeder simulations. Fourth, cross-tool and model-validation studies emphasise the need for consistent benchmark transfer between network and dynamic environments [13–15], yet they do not usually combine feeder time-series, disturbance selection, and reduced-order frequency screening within one coordinated study chain.

Accordingly, the gap addressed here is not the absence of individual voltage, inertia, or controller studies, but the limited availability of a single planning workflow that links feeder operating conditions, disturbance selection from feeder time-series data, and reduced-order frequency-security screening. Previous studies commonly assessed steady-state hosting behaviour and post-disturbance frequency response separately while some other studies impose frequency events that are not derived from the feeder operating trajectory. This study addresses that practical gap by evaluating a renewable-rich IEEE 33-bus feeder with embedded photovoltaic (PV), wind generation, and a grid-forming BESS within one coordinated feeder-to-frequency workflow. The active-power deficit used in the dynamic study is taken from the largest hourly reduction in aggregated PV and wind output obtained from the 24 h feeder simulation, rather than from a heuristically imposed external event. In this way, the feeder operating state and the post-disturbance frequency study remain physically consistent while the overall analysis stays within a planning-level screening scope.

Therefore, the main objectives of this study are to: (i) assess the steady-state performance of a renewable-rich IEEE 33-bus distribution feeder under increasing renewable penetration; (ii) derive a physically consistent disturbance from feeder time-series data for post-disturbance frequency-security assessment; and (iii) evaluate the extent to which a grid-forming battery energy storage system, through droop control, synthetic inertia, and fast frequency response, can improve frequency performance under renewable-drop events. The specific contributions of this study are as follows:

1. The first contribution is a cross-checked feeder-to-frequency assessment workflow that combines PowerFactory, Pandapower, OpenModelica, and PSAT to connect feeder operating conditions with reduced-order frequency-security screening. The added value of this combination is that each tool has a distinct verification role: PowerFactory provides the main feeder model and time-series operating assessment, Pandapower provides an independent open-source steady-state voltage cross-check, OpenModelica implements the transparent equation-based reduced-order frequency model, and PSAT serves as an independent dynamic benchmark. This reduces dependence on a single simulation environment while preserving a traceable data chain from feeder operation to frequency-security screening.
2. The second contribution is a quantified planning interpretation of the monotonic changes in feeder losses, maximum loading, and the upper-voltage envelope under the selected DER placements and common peak-load operating condition.

3. The third contribution is a controller assessment that quantifies the effect of BESS droop and fast frequency response under disturbance magnitudes extracted from feeder time-series data, while aggregate inertial behaviour is represented consistently through the equivalent swing-equation parameter.

The remainder of this paper is organized as follows. Section 2 presents the feeder model and cross-platform assessment workflow. Section 3 develops the reduced-order grid-forming BESS model and defines its range of validity. Section 4 describes the penetration cases, disturbance extraction, and compliance criteria. Section 5 presents and discusses the steady-state and frequency-security results. Section 6 concludes the paper and outlines future work.

2. Feeder Model and Cross-Platform Assessment Framework

2.1. Test Feeder and Base Data

The study system is the IEEE 33-bus radial feeder [3], implemented in DIgSILENT PowerFactory as a 12.66 kV radial distribution network supplied from an upstream 33 kV grid through a step-down transformer. Loads are represented as constant-power demands, and the common feeder peak-load base used for the penetration study is 2.006 MW. As presented in Figure 1, the distributed photovoltaic (PV) units are positioned at buses 6, 18, and 30, while the doubly fed induction generator (DFIG)-based wind generation is placed at buses 14 and 25. In the archived feeder-study dataset, the installed renewable capacity totals 1.041 MW of PV across buses 6, 18, and 30 and 0.225 MW of DFIG-based wind generation across buses 14 and 25. Additionally, the BESS is connected at bus 33 through a bidirectional grid-forming converter. The same feeder topology, bus allocations, and penetration cases are transferred to Pandapower for steady-state cross-checking, while the time-series-derived disturbance magnitudes are passed to the reduced-order OpenModelica and PSAT frequency model. This separation keeps the feeder-side operating assessment and the frequency-side screening logically consistent while preserving a common data chain across tools. The principal feeder, disturbance, and dynamic-study assumptions used for reproducibility are summarized in Table 1.

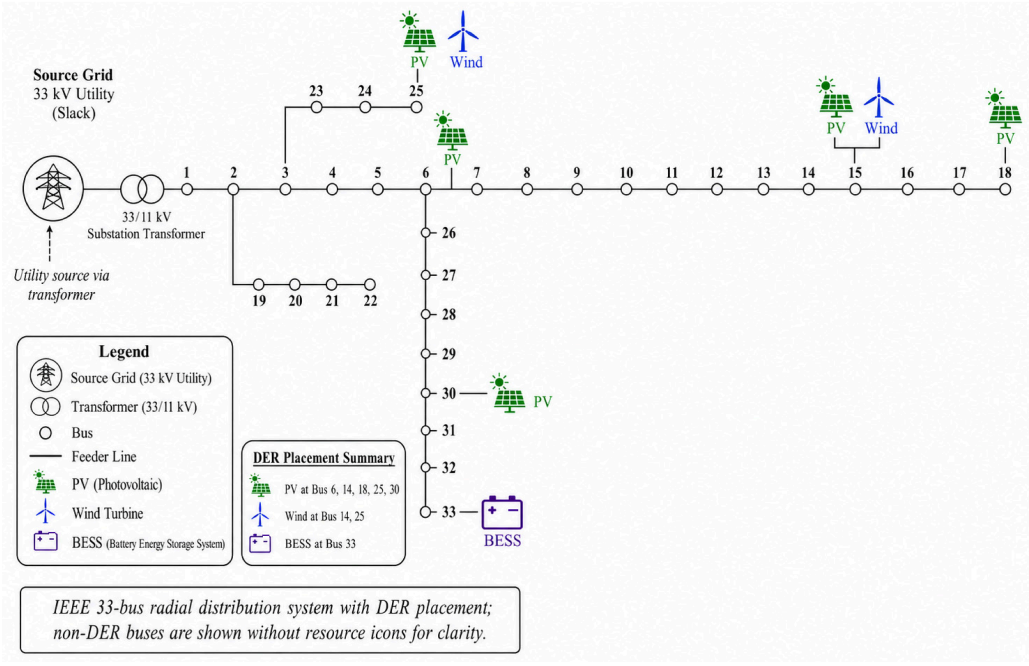


Figure 1. Single-line diagram of the IEEE 33-bus feeder showing the locations of the PV, wind, and BESS units.

Table 1. Compact base-data and modelling assumptions used for reproducibility.

Benchmark Feeder	**IEEE 33-Bus Radial Feeder [3]**	**Benchmark Feeder**
Upstream/feeder voltage	33/12.66 kV step-down supply to the radial feeder	Upstream/feeder voltage
Load model and common base	Constant-power loads; common feeder peak-load base = 2.006 MW	Load model and common base
Line and transformer data source	Standard IEEE 33-bus benchmark data [3] with the study transformer represented in PowerFactory	Line and transformer data source
PV allocation	Buses 6, 18, and 30	PV allocation
Wind allocation	DFIG-based wind generation at buses 14 and 25	Wind allocation
BESS allocation	Grid-forming BESS connected at bus 33	BESS allocation
Renewable penetration cases	0%, 10%, 25%, 50%, 75%, and 100% of feeder peak load	Renewable penetration cases
Time-series/disturbance basis	Hourly PowerFactory feeder exports used to identify renewable-deficit stress magnitudes	Time-series/disturbance basis
Reduced-order dynamic base	10 MVA, 50 Hz base with Thevenin-based coupling derived at the BESS terminal	Reduced-order dynamic base
BESS power assumption	Primary support case: P_0 = 0 MW with ±2 MW reserved active-power headroom; comparison case: ±1 MW headroom	BESS power assumption
BESS energy basis	Short-duration reserve adequacy assumed for the reported sub-2 s nadir events; no separate MWh optimization	BESS energy basis
PV installed capacity	1.041 MW total across buses 6, 18, and 30 in the archived feeder-study dataset	PV installed capacity
Wind installed capacity	0.225 MW total across buses 14 and 25 in the archived feeder-study dataset	Wind installed capacity
Detailed numerical data	Per-bus load data, component ratings, transformer representation, and archived hourly profile files are provided in the GitHub repository listed in the Data Availability Statement	Detailed numerical data
Dynamic disturbance conversion	Renewable deficits are extracted in MW and converted using $\Delta P_{pu} = -\Delta P_{MW}/S_{base}$, with S_{base} = 10 MVA. The 75% and 100% severe events are −0.0305 pu and −0.0406 pu, respectively.	Dynamic disturbance conversion
Thevenin transfer quantities	For the 12.66 kV, 10 MVA base, $Z_{base} = V_{base}^2/S_{base}$ = 16.03 Ω. At the BESS/PCC terminal, $Vth = V_{PCC} + Zth\, I_{PCC}$, $X_{eq} = \mathrm{Im}\{Zth_{,33}\}/Z_{base}$, and $K_s = (E\, V_g/X_{eq}) \cos \Delta_0$. The time-domain screening uses the aggregate swing-equation channel.	Thevenin transfer quantities

An explicit short-circuit-ratio sweep is not reported because the archived study files were developed around the Thevenin-based reduced-order representation rather than a separate SCR parameter study. Accordingly, the manuscript does not introduce an unsupported numerical SCR claim; instead, the synchronizing term in the reduced-order model is derived from the positive-sequence Thevenin reactance seen from the BESS terminal, and dedicated grid-strength sensitivity is reserved for future work. Detailed component ratings, the standard IEEE 33-bus per-bus load allocation, and the archived hourly profile files used in the workflow are provided in the project repository identified in the Data Availability Statement.

2.2. Cross-Tool Validation Methodology

Cross-tool validation was completed before the penetration results were interpreted. This step was used to distinguish physical trends from software-transfer or implementation errors. In the steady-state stage, PowerFactory and Pandapower used their built-in Newton–Raphson load-flow solvers on the same feeder data without non-default convergence overrides. In the dynamic stage, archived OpenModelica and PSAT cases were

executed on a common 10 MVA, 50 Hz base with the same event timing, a 0.02 s reporting interval over a 6–8 s horizon, and a 0.10 s post-event RoCoF window. The cross-tool benchmark as a solver-behaviour check, whereas the corrected feeder-event magnitudes and scenario results are reported separately in the Results and Discussion section.

Stage 1—Steady-state validation: The load-flow results obtained in PowerFactory were reproduced in Pandapower [16,17] using the same feeder data, bus allocations, and DER placements. Voltage-magnitude results were compared against the acceptance limits in Table 2, while Pandapower was retained primarily as a supporting voltage-focused cross-check and weak-bus consistency check rather than as the primary source for all loading and loss claims.

Table 2. Steady-state cross-tool validation limits and the deviations obtained.

Achieved Deviation	Maximum Deviation	Parameter
0.0155 pu	2%	Voltage magnitude

Stage 2—Frequency validation: The reduced-order OpenModelica model was compared with an archived PSAT implementation under a common benchmark disturbance [18]. RoCoF, nadir, and settling time were evaluated to check the transfer of the reduced-order dynamics before scenario screening. Nadir and settling time are treated as the primary agreement metrics, while RoCoF is interpreted conservatively because it is more sensitive to solver time step, numerical differentiation, and event realization.

Stage 3—Disturbance consistency: The 24 h feeder simulation in PowerFactory was exported to Python 3.10, where the combined PV and wind profiles were checked to identify the largest hourly drop in renewable power for each scenario set. That event size was then used in the reduced-order frequency model. This ensures that the dynamic study remains tied to the actual operating conditions produced by the feeder model and avoids the use of an assumed external disturbance.

3. Grid-Forming BESS Model for Inertia Emulation and Fast Frequency Response

3.1. Virtual Synchronous Machine Model

The grid-forming BESS is represented using a reduced-order virtual synchronous machine model [5,10–12,19]. The model is intended for planning-level screening and captures the main active-power and frequency behavior of interest. It is deliberately simplified by using the equivalent swing-equation behavior in (1), together with synchronizing power, damping, and active-power support terms, so that different penetration cases and controller settings can be compared clearly.

$$\frac{2H_{\text{vir}}}{\omega_s}\frac{d\omega}{dt} = P_m - P_e - D(\omega - \omega_s) \quad (1)$$

In this model, H_{vir} is the virtual inertia constant in seconds, D is the damping coefficient in pu/Hz, ω_s is the synchronous speed in rad/s, P_m is the active-power reference in pu, P_e is the electrical output power in pu, and ΔP_{sup} is the supplementary active-power support term. Where an equivalent inertia-channel gain K_i is used internally, it is set consistently with H_{vir}. For consistency in reporting, H_{vir} is used as the main inertia quantity throughout the paper.

The coupling between the converter and the grid is represented by (2), the standard power-angle relation across an equivalent reactance. This is enough to capture the syn-

chronizing effect needed for reduced-order small-signal analysis, without including extra electromagnetic detail that is not necessary for this planning study.

$$P_e = \frac{EV_g}{X_{\text{eq}}}\sin(\delta) \tag{2}$$

Linearizing the model around the operating point gives a compact state-space form that is suitable for comparing different disturbance scenarios and support settings.

$$\Delta P_e = K_s \Delta\delta, \quad K_s = \frac{EV_g}{X_{\text{eq}}}\cos(\delta_0) \tag{3}$$

K_s represents the synchronizing-power coefficient. The same notation is used throughout the state-space model and the related sensitivity analysis.

3.2. State-Space Representation

Using the state vector shown in (4), the small-signal model provides a practical way to examine eigenvalues, carry out parametric studies, and compare frequency responses in the time domain.

$$\dot{\mathbf{x}} = \mathbf{A}\mathbf{x} + \mathbf{B}\Delta P_m, \quad \mathbf{x} = [\Delta\delta\ \Delta\omega]^{\mathrm{T}} \tag{4}$$

where

$$\mathbf{A} = \begin{bmatrix} 0 & 1 \\ -\frac{\omega_s K_s}{2H_{\text{vir}}} & -\frac{\omega_s D}{2H_{\text{vir}}} \end{bmatrix}, \quad \mathbf{B} = \begin{bmatrix} 0 \\ \frac{\omega_s}{2H_{\text{vir}}} \end{bmatrix} \tag{5}$$

The eigenvalues of the state matrix determine the small-signal stability of the reduced-order model.

$$\lambda_{1,2} = -\frac{\omega_s D}{4H_{\text{vir}}} \pm \sqrt{\left(\frac{\omega_s D}{4H_{\text{vir}}}\right)^2 - \frac{\omega_s K_s}{2H_{\text{vir}}}} \tag{6}$$

For positive synchronizing power and damping, the linearized model remains asymptotically stable. Within this paper, the model is not used to represent electromagnetic transients or converter inner-loop protection phenomena; rather, it is used as a planning-oriented frequency-security screening model.

3.3. Aggregate Inertia, Droop, and Fast Frequency Response

The general reduced-order support representation combines aggregate inertia, droop action, and fast frequency response. In the implemented OpenModelica scenario cases, aggregate inertial behaviour is represented by the swing-equation parameter H, while the supplementary BESS command is provided by droop and FFR channels. This separation allows the effect of proportional and rapid active-power support to be evaluated without implying a detailed converter inner-loop model.

$$\Delta P_{\text{SI}} = -K_d(f - f_0) - K_i\frac{df}{dt} \tag{7}$$

In the general control law, K_d denotes the droop gain, K_i denotes a derivative-channel coefficient that can be associated with inertia emulation, and K_{FFR} denotes the fast-frequency-response gain. In the reported time-domain implementation, a separate derivative support command is not varied; instead, the equivalent inertia is represented by H = 4.0 s in the swing equation, while droop and FFR act through filtered and saturation-limited supplementary power channels.

The FFR block includes a deadband, first-order response dynamics, an activation-duration limit, and an active-power saturation limit. These elements prevent the reduced-order model from implying unlimited instantaneous support. The formulation does not

include a manufacturer-specific millisecond delay, detailed current-limiter dynamics, or round-trip efficiency; such implementation details are outside the planning-level scope.

$$\Delta P_{\mathrm{FFR}} = -K_{\mathrm{FFR}}(f - f_0), \quad |f - f_0| > f_{\mathrm{db}}; \qquad \Delta P_{\mathrm{FFR}} = 0, \quad \text{otherwise} \tag{8}$$

The final support action is therefore constrained by the droop and FFR response time constants and by the individual and total active-power limits.

The total converter power command is obtained by superimposing the support terms on the pre-disturbance set-point.

$$P_{\mathrm{ref}} = P_0 + \Delta P_{\mathrm{SI}} + \Delta P_{\mathrm{FFR}} \tag{9}$$

where P_0 denotes the pre-disturbance operating point of the BESS.

3.4. Physical Interpretation of the Loss Trend and Model Scope

For the studied feeder, DER placement, and common peak-load operating condition, the reported penetration results show a monotonic increase in total feeder losses as renewable penetration increases. This behavior is interpreted as a feeder-specific planning result rather than as a universal theorem. In the selected cases, additional downstream renewable injection increases branch-current redistribution and reverse-power-flow exposure, causing I^2R losses to rise even though the minimum bus voltage remains close to 1.0 pu.

Accordingly, the observed loss trend should be understood as dependent on DER placement, loading pattern, dispatch level, and network resistance distribution. The interpretation is included to explain the trend seen in this feeder and should not be generalized as a closed-form result for all radial feeders.

Likewise, the reduced-order model is applied only within the limits of its intended scope. It represents the dominant frequency-active-power channel seen by the upstream system when the feeder experiences a net renewable-output deficit, and it is used here for planning-level comparison of RoCoF, nadir, and settling time across scenarios. The feeder is represented in balanced positive sequence, and the model does not resolve electromagnetic transients, converter inner-loop dynamics, detailed PLL behavior, converter over-current limitation, protection interactions, or battery state-of-charge and energy-depletion effects over long horizons. Accordingly, the dynamic results should be interpreted as planning-level screening outcomes under idealized short-duration support availability. For that reason, the model is benchmarked against PSAT and used conservatively as a reduced-order security-assessment tool rather than as a substitute for higher-fidelity EMT studies.

3.5. Aggregation, Base Values, and Converter Limits

To make the reduced-order model reproducible, the net renewable active-power deficit is first extracted from the feeder time-series in MW and then referred to a common reduced-order base. The frequency simulations use S_{base} = 10 MVA, f_0 = 50 Hz, and an equivalent aggregate inertia H = 4.0 s. Feeder-base per-unit values are retained only as screening indicators. Prior to the simulation, each MW deficit is converted using $\Delta P_{pu} = -\Delta P_{MW}/S_{base}$. Accordingly, the severe 75% and 100% events correspond to -0.0305 pu and -0.0406 pu, respectively, on the dynamic-system base. Using one explicit base for the disturbance, inertia, damping, droop, FFR gains, and BESS limits removes the per-unit ambiguity identified during review.

For the small-signal state-space interpretation in (2) and (3), the network coupling is obtained from the positive-sequence Thevenin impedance seen from the BESS/PCC terminal after reducing the feeder to an upstream-source/equivalent-DER interface. The Thevenin equivalent at the PCC is expressed as $Vth = V_{PCC} + Zth\, I_{PCC}$, with $Zth = Rth + \mathrm{j}X_{th}$.

On the 12.66 kV, 10 MVA base, $Z_{base} = V_{base}^2 / S_{base} = 16.03\ \Omega$, $X_{eq} = \mathrm{Im}\{Zth_{,33}\}/Z_{base}$, and $K_s = (E\ V_g / X_{eq}) \cos \delta_0$. These quantities are important because the equivalent reactance controls synchronizing stiffness and reduced-order inertial response, while the common base ensures that the extracted disturbance, inertia, damping, and BESS support limits are all referred to the same dynamic-system base. The scenario time-domain simulations use the aggregate frequency channel, while feeder resistance and branch-level voltage and loss effects remain in the PowerFactory and Pandapower models.

Because the archived study files were not organized as a separate grid-strength sensitivity package, the manuscript does not introduce an unsupported numerical short-circuit-ratio estimate. The present dynamic results should therefore be interpreted as planning-level frequency-screening outcomes for the adopted Thevenin equivalent at the BESS terminal rather than as a dedicated weak-grid stability-boundary study.

In the dynamic cases, the phrase "2 MW droop" denotes 2 MW of reserved active-power support headroom, not an unlimited command. The BESS is initialized at $P_0 = 0$ MW, and the controller parameters are converted to the same 10 MVA base as the disturbance. The filtered droop and FFR commands are formed separately, limited by their allocated headroom, summed, and then passed through the common total-power saturation. Consequently, neither channel is given priority after the total converter limit is reached. Battery state of charge is assumed adequate over the reported short-duration nadir window; no separate MWh optimization or long-horizon depletion model is applied.

Specific manufacturer ramp-rate values, current-limit dynamics, and round-trip efficiency are not imposed explicitly. Instead, the time constants $T_{droop} = 0.40$ s and $T_{FFR} = 0.01$ s represent aggregate response dynamics, while the individual and total saturation limits represent available short-duration active-power capability. Detailed converter current control, protection, efficiency, and energy depletion should therefore be examined in EMT or hardware-in-the-loop studies.

4. Case Studies, Disturbance Extraction, and Compliance Criteria

4.1. Penetration Scenarios

Renewable penetration is examined at 0%, 10%, 25%, 50%, 75%, and 100% of feeder peak load by scaling DER ratings while maintaining the same load level across scenarios. All steady-state penetration scenarios were compared at the same feeder load condition, taken as the feeder peak-load base, while only the renewable generation level was varied across cases. This ensures that differences in voltage profile, feeder losses, and frequency-security metrics are attributable to renewable penetration rather than to changes in demand. The BESS operates in grid-forming mode in every case so that changes in the reported dynamic metrics are attributable primarily to renewable-penetration level, extracted disturbance magnitude, and controller support settings.

4.2. Disturbance Extraction from Time-Series

The 24 h PowerFactory simulation provides hourly PV and wind output profiles for each scenario from the archived feeder-study dataset. In the revised workflow, these hourly profiles are not interpreted as literal second-by-second frequency events. Instead, adjacent hourly operating points are used to identify the most severe renewable-output deficit magnitude for each penetration level, and that extracted deficit is then imposed in the reduced-order frequency model as a conservative planning-level stress test. For each penetration level, the time-series export is used to map mild, moderate, and severe renewable-deficit cases, and the severe case is then transferred to the reduced-order frequency model. At 75% penetration, the representative severe operating-point change occurs at hour 18, when PV output falls from 0.3219 MW to 0 MW while wind output changes from

0.2007 MW to 0.2178 MW, producing a net renewable drop of 0.3048 MW. This corresponds to −0.1519 pu on the feeder peak-load screening base and to −0.0305 pu after conversion to the common 10 MVA dynamic base. This procedure keeps the stress magnitude tied to the actual feeder operating profile while avoiding an externally imposed or heuristic event.

$$P_{\mathrm{RES}}(k) = P_{\mathrm{PV}}(k) + P_{\mathrm{wind}}(k) \tag{10}$$

$$\Delta P_{\mathrm{step}} = \min_{k} \left[P_{\mathrm{RES}}(k) - P_{\mathrm{RES}}(k-1)\right], \quad \Delta t = 1\,\mathrm{h} \tag{11}$$

With Δt = 1 h, ΔP_{step} is extracted as the minimum first difference in aggregated renewable power across adjacent hourly operating points. Negative values therefore denote renewable-output drops, and the most negative value defines the severe hourly derived deficit magnitude used in the reduced-order model. The hourly difference determines the size of the imposed imbalance; it is not a physical representation of the actual intra-hour renewable ramp. In the reported screening cases this extracted deficit is applied as a step, which is a conservative planning assumption relative to a linear one-hour ramp of the same final magnitude. For example, at 75% penetration the severe-event magnitude is $|\Delta P|$ = 0.3048 MW; applying it as a step gives a first-interval energy exposure of 0.3048 MWh, whereas an equivalent linear one-hour ramp yields 0.1524 MWh. The step approximation therefore doubles the first-interval deficit exposure relative to the ramp case and is retained as the conservative planning-level screening representation; finer sub-second disturbance reconstruction would require higher-resolution renewable data and EMT-level modelling.

The hourly extraction interval reflects the resolution of the renewable-generation profiles available in the archived feeder-study workflow. Accordingly, the feeder time-series simulation is used to identify the magnitude of a severe renewable-output reduction between adjacent operating points, while the reduced-order frequency model is used to test whether the available active-frequency support remains adequate when that extracted deficit is imposed as a conservative stress case. The hourly deficit magnitude therefore represents the severe sustained power imbalance that challenges primary frequency response and BESS headroom, not the sub-second ramp rate of individual cloud transients or wind gusts. Because the actual ramp within the hour would be slower than the idealized step representation applied in the screening study, the resulting nadir estimates should be interpreted as conservative, planning-level outcomes. Finer temporal resolution would require sub-hourly renewable data together with EMT-level converter modelling and is therefore reserved for future work. In the penetration-comparison workflow, the common feeder peak-load base is retained while the hourly renewable export sequence defines the operating-point changes used for disturbance screening; therefore, the reduced-order frequency cases do not introduce an additional independent stochastic load-variation sweep beyond the archived feeder operating sequence.

4.3. Compliance Screening Matrix

The screening limits in this study are based on the Nigerian Grid Code [20] and IEEE 1547-2018 [21], as summarized in Table 3, with international context provided in Table 4. The Nigerian Grid Code was selected as the primary benchmark because the study was designed to inform distribution planning in the Nigerian 50 Hz power-system context, where renewable integration is expanding and frequency-security margins are critical. IEEE 1547-2018 is included only as a comparative 60 Hz distributed-energy-resource interconnection reference and is not treated as the governing compliance standard for the Nigerian feeder case. The limits are used as acceptance checks for voltage magnitude,

frequency range, and under-frequency ride-through, while also providing a basis for interpreting the available security margin.

Table 3. Compliance screening matrix.

Evidence	Screening Criterion	Requirement
Dynamic traces	49.75–50.25 Hz	Normal frequency
Nadir values	>48.75 Hz	Under-frequency ride-through
Steady-state metrics	0.95–1.05 pu	Voltage (11 kV)
24 h maximum	<1.10 pu for 120 s	Overvoltage

Table 4. Comparative compliance screening matrix.

Typical European [22]	Ethiopian Grid Code [23]	IEEE 1547-2018 [21] (60 Hz Context)	Nigerian Grid Code [20] (50 Hz Basis)	Requirement
49.5–50.5	49.0–51.0	57.0–60.5	49.75–50.25	Normal frequency (Hz)
>47.5	>47.0	Varies	>48.75	Frequency ride-through limit (Hz)
0.90–1.10	0.90–1.10	0.88–1.10	0.95–1.05 [24]	Voltage (11 kV, pu)
<1.10	<1.15	<1.10	<1.10 for 120 s	Overvoltage limit (pu)

5. Results and Discussion

5.1. Cross-Tool Validation Results

5.1.1. Steady-State Validation (PowerFactory vs. Pandapower)

Table 5 lists the steady-state validation results between PowerFactory and Pandapower at four selected buses in the benchmark load-flow case. The comparison is carried out at buses with connected PV and BESS resources so that the cross-tool transfer is checked at electrically relevant locations. This benchmark validation case is separate from the regulated penetration sequence; therefore, Table 5 is used as a solver-transfer check, while the penetration results are used for the planning interpretation of the penetration trend. The largest mismatch occurs at Bus 33, the BESS terminal, where the error is 1.6203%. This value is below the 2% validation threshold used in Table 2 but is reported explicitly because Bus 33 is electrically sensitive; therefore, the BESS-terminal voltage results are interpreted conservatively. Accordingly, Pandapower is used primarily as a voltage-focused steady-state cross-check, while PowerFactory remains the primary source for feeder losses, loading, disturbance mapping, and the 24 h operating assessment.

Table 5. Steady-state validation results between PowerFactory and Pandapower.

Error (%)	V_PP (pu)	V_PF (pu)	Bus
0.3492	0.9737	0.9703	6
0.8798	0.9548	0.9632	18
0.1042	0.9594	0.9584	30
1.6203	0.9566	0.9721	33

5.1.2. Frequency Validation (PSAT vs. OpenModelica)

For the common cross-tool benchmark case, OpenModelica and PSAT show close agreement in frequency nadir and settling time, while the RoCoF comparison gives a larger deviation. RoCoF is therefore not presented as close agreement; it is used to demonstrate

the sensitivity of the initial-frequency slope to solver time step, numerical differentiation, and event implementation. This validation supports planning-level trend screening and relative scenario comparison, but it is not a substitute for EMT simulation, converter-level validation, PLL stability assessment, hardware-in-the-loop testing, or protection-coordination studies. The corrected feeder-event results are reported separately in the Results and Discussion section.

The absolute RoCoF difference between PSAT and OpenModelica is 0.111 Hz/s, corresponding to the 17.33% mean absolute percentage error (MAPE) reported in Table 6. This discrepancy is attributed to early-time sensitivity in the RoCoF calculation, particularly the numerical differentiation window, solver time step, and exact realization of the applied power step. The interpretation of the frequency benchmark therefore emphasizes nadir and settling time, while RoCoF is treated as a conservative indicator rather than as a precise protection-setting value.

Table 6. Frequency-validation metrics for the common cross-tool benchmark case.

MAPE (%)	OpenModelica	PSAT	Metric
17.33	0.529925	0.641	RoCoF (Hz/s)
0.138	49.9631	49.894	Nadir (Hz)
1.16	1.396	1.38	Settling time (s)

5.2. Steady-State Penetration Results

Table 7 depicts steady-state results for all penetration cases under a common feeder peak-load base; therefore, the observed trend reflects the effect of increasing DER penetration under the same demand condition.

Table 7. Steady-state metrics for the 0–100% renewable-penetration sequence.

Max Loading (%)	Losses (MW)	Vmax (pu)	Vmin (pu)	Penetration (%)
11.69	0.0246	1.0295	0.9999	0
13.62	0.0321	1.0351	0.9998	10
16.50	0.0457	1.0434	0.9997	25
21.24	0.0744	1.0568	0.9996	50
25.91	0.1103	1.0699	0.9994	75
30.52	0.1531	1.0826	0.9991	100

Table 7 presents three important observations for planning. First, the minimum feeder voltage remains close to 1.0 pu across all penetration cases, decreasing only slightly from 0.9999 pu at 0% penetration to 0.9991 pu at 100% penetration. Second, the upper voltage envelope increases with penetration, with Vmax rising from 1.0295 pu to 1.0826 pu, indicating the expected voltage-rise effect caused by increased renewable power injection. Third, feeder losses increase from 0.0246 MW to 0.1531 MW, while maximum loading rises from 11.69% to 30.52%. The increase in maximum loading is justified by the higher power flow through feeder components as renewable penetration increases. Since the maximum loading remains below 100% in all cases, the feeder does not experience thermal overloading, although the reduction in loading margin indicates greater network utilisation at higher penetration levels.

The branch-level thermal evidence is summarized compactly by the maximum-loading column in Table 7 and by the limiting element reported in the 24 h summary in Table 8. The maximum loading increases from 11.69% to 30.52% as penetration rises from 0% to 100%,

confirming that the loss increase is accompanied by higher current utilization in at least one branch or transformer path. The full branch-current output is available in the project data repository, while the manuscript reports the maximum-loading indicator to avoid a long branch-by-branch table. The corresponding voltage and loss trends are illustrated in Figures 2 and 3, respectively.

Table 8. 24 h operating assessment across penetration levels.

Pen. (%)	MinV_24 h (pu)	MaxV_24 h (pu)	MaxLoad_24 h (%)
0	0.9999	1.0295	11.69
10	0.9998	1.0343	13.30
25	0.9998	1.0414	15.70
50	0.9997	1.0531	19.65
75	0.9995	1.0644	23.55
100	0.9993	1.0755	27.40

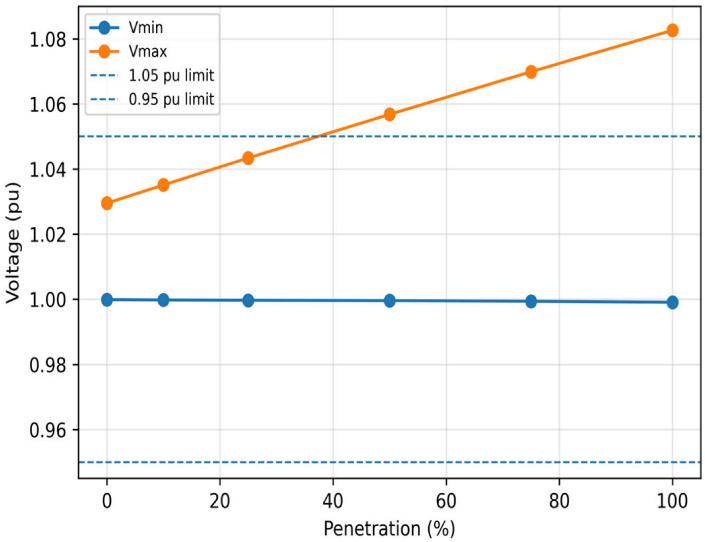


Figure 2. Steady-state minimum and maximum voltage versus renewable penetration.

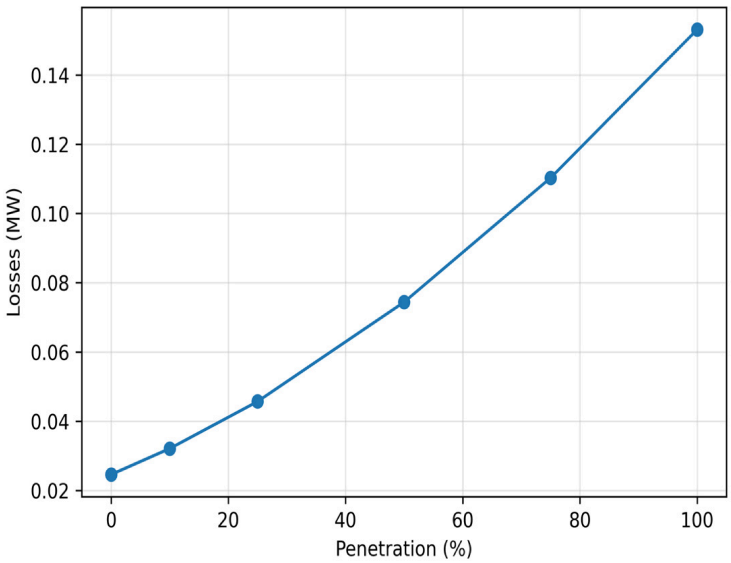


Figure 3. Feeder losses versus renewable penetration.

5.3. Time-Series Operating Assessment

The 24 h assessment demonstrates that one snapshot alone is not enough to understand renewable-rich feeder performance, as shown in Table 8. At 75% penetration, the daily profile reaches a maximum voltage of 1.0644 pu and a maximum loading of 23.55%, while the minimum feeder voltage remains close to 1.0 pu at 0.9994 pu. The wider daily sweep across all penetration levels shows that Min(V) over 24 h remains close to 1.0 pu, whereas Max(V) over 24 h rises from 1.0295 pu at 0% penetration to 1.0755 pu at 100% penetration, and the maximum daily loading increases from 11.69% to 27.40%. The maximum daily voltage is slightly lower than the corresponding steady-state Vmax values in Table 7 because Table 7 represents the regulated penetration snapshot, whereas the daily assessment reflects time-varying renewable output and does not necessarily reach the same simultaneous rated-output condition. This confirms that over-voltage mitigation and storage dispatch may still be necessary during periods of high renewable output and low local demand. The 75% daily voltage trajectory is illustrated in Figure 4.

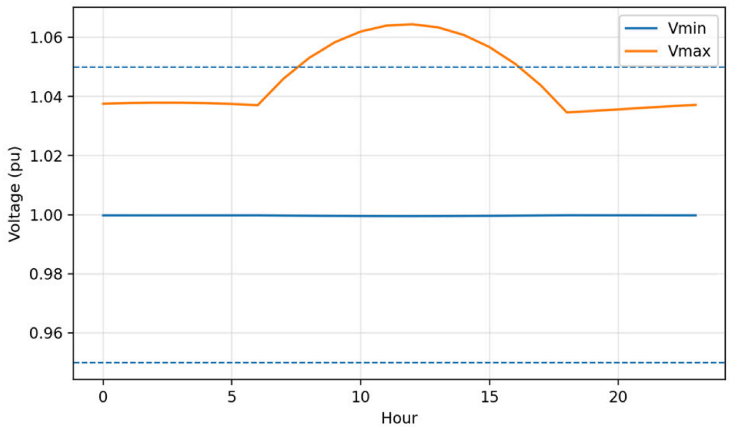


Figure 4. Daily evolution of feeder minimum and maximum voltage at 75% penetration. Dotted horizontal lines indicate the 0.95 and 1.05 pu voltage limits.

5.4. Frequency Security Under Renewable-Drop Events

Table 9 presents the dynamic frequency metrics for the 75% severe hourly derived renewable-deficit stress case (ΔP = 0.3048 MW; converted dynamic-model input ΔP_{step} = −0.0305 pu on the 10 MVA base).

Table 9. Dynamic frequency metrics for the 75% severe hourly renewable-drop event.

Nadir Improvement	Settling Time (s)	Nadir (Hz)	RoCoF (Hz/s)	Case
—	1.18	49.9695	0.1681	Baseline (no support)
9.9 mHz	1.28	49.9794	0.1681	2 MW droop only
22.9 mHz	1.00	49.9924	0.1681	2 MW droop + FFR

For the 75% severe hourly derived renewable-deficit event, the corrected input is 0.3048 MW, equivalent to −0.0305 pu on the 10 MVA base. Without supplementary support, the frequency nadir is 49.9695 Hz. Droop support improves the nadir to 49.9794 Hz, while droop plus FFR increases it to 49.9924 Hz. The corresponding nadir improvements are 9.9 mHz and 22.9 mHz. The similar 0.10 s-window RoCoF values occur because the initial slope is dominated by the same applied power imbalance and aggregate inertia before the filtered support channels develop fully. The droop-plus-FFR case settles within the ±0.01 Hz final-value band at approximately 1.00 s. Table 10 and Figure 5 show that, as penetration rises, the converted severe-event magnitude increases from 0.0041 pu at 10%

penetration to 0.0406 pu at 100%, and the supported nadir declines from 49.9959 Hz to 49.9898 Hz. All supported cases remain above the adopted normal-frequency lower bound, although the margin decreases with penetration.

Table 10. Penetration-dependent frequency response under 2 MW droop + FFR.

Settling Time (s)	Nadir (Hz)	RoCoF (Hz/s)	Dynamic ΔP_{step} (pu, 10 MVA)	Penetration (%)
1.00	50.0000	0.0000	0.0000	0
1.00	49.9959	0.0224	−0.0041	10
1.00	49.9944	0.0560	−0.0102	25
1.00	49.9941	0.1120	−0.0203	50
1.00	49.9924	0.1681	−0.0305	75
1.00	49.9898	0.2241	−0.0406	100

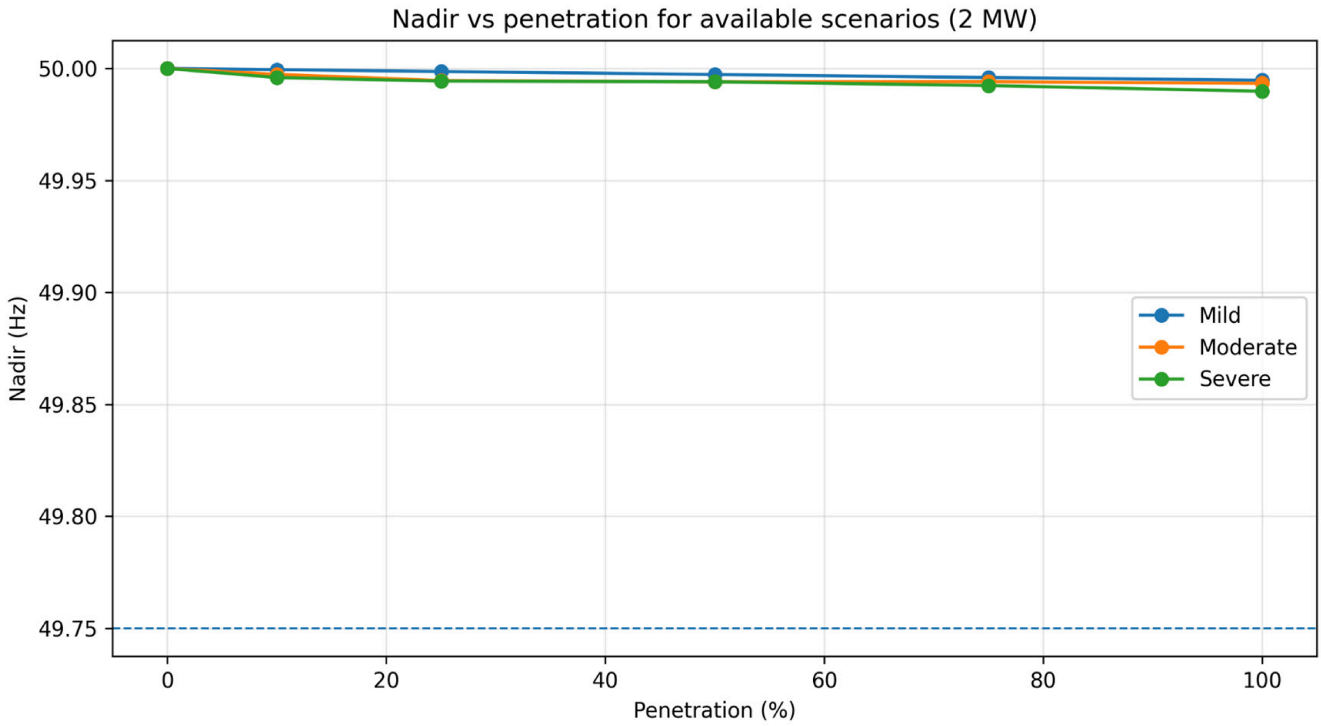


Figure 5. Frequency nadir versus renewable penetration for mild, moderate, and severe disturbances under 2 MW droop plus FFR. The dotted horizontal line indicates the 49.75 Hz lower normal-frequency screening limit.

When the dynamic results are compared with the steady-state limits, upper voltage is the earliest binding screening constraint in this feeder. The supported frequency nadirs remain above the normal lower bound, and maximum loading remains far below 100%; however, the 1.05 pu voltage limit is exceeded from the 50% penetration snapshot onward in Table 7. This reinforces the need to assess voltage, loading, and frequency security together rather than treating any single metric as sufficient.

5.5. BESS Headroom and Controller Interpretation

The corrected simulations indicate that controller response and available headroom must be interpreted together. In the 2 MW case, the droop and FFR commands remain subject to their response time constants and active-power limits; however, the corrected severe disturbances are not large enough to saturate either the 1 MW or 2 MW total

headroom. Accordingly, the size comparison is used as a headroom-adequacy check rather than as evidence that capacity is unimportant. For practical deployment, BESS size, reserve policy, feeder strength, voltage requirements, energy duration, and project economics should be assessed jointly [25]. Under the present planning assumptions, voltage mitigation becomes necessary before the tested BESS headroom becomes binding.

The corrected BESS-size comparison shows that 1 MW and 2 MW reserved active-power headroom produce practically identical metrics for the investigated severe events. At 75% penetration, both cases give RoCoF = 0.1681 Hz/s, nadir = 49.9924 Hz, and settling time = 1.00 s. This occurs because the commanded droop-plus-FFR support remains below the 1 MW saturation limit; therefore, increasing the available headroom to 2 MW does not change the response. This result is scenario-specific and should not be interpreted as a general conclusion that BESS size is unimportant. The BESS-size comparison is summarized in Table 11, and the corresponding severe-case nadir comparison is shown in Figure 6.

Table 11. BESS-size comparison for the corrected 75% severe renewable-deficit event on the 10 MVA base.

Settling Time (s)	Nadir (Hz)	RoCoF (Hz/s)	BESS Headroom (MW)
1.00	49.9924	0.1681	1.00
1.00	49.9924	0.1681	2.00

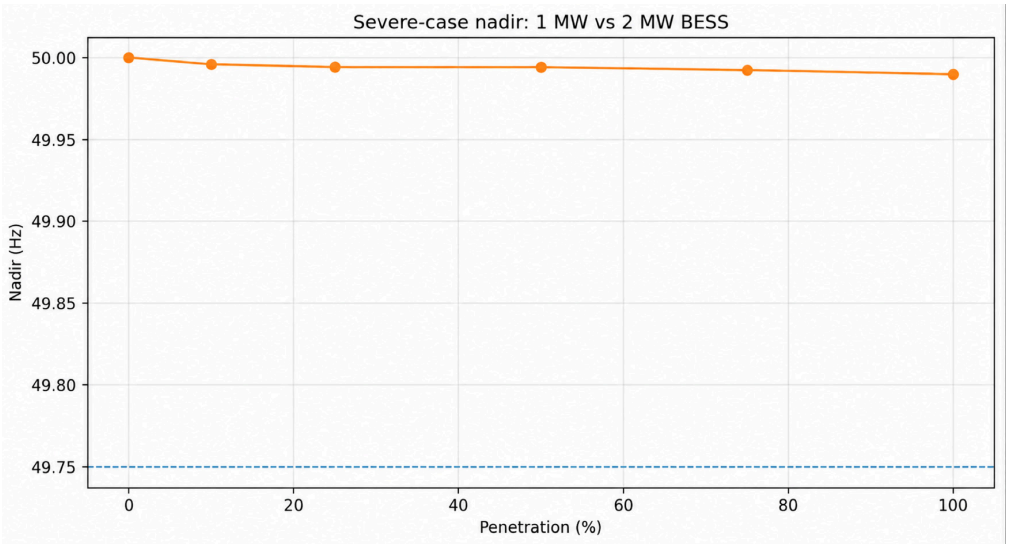


Figure 6. Severe-case frequency nadir versus renewable penetration for 1 MW and 2 MW reserved BESS headroom. The dotted horizontal line indicates the 49.75 Hz lower normal-frequency screening limit.

6. Conclusions and Future Work

This paper presented a cross-checked planning-level workflow that integrates DIgSILENT PowerFactory, Pandapower, OpenModelica, and PSAT to assess feeder operation and post-disturbance frequency security within one traceable study chain. The literature contribution is the workflow integration and disturbance-transfer procedure rather than a new control or optimization algorithm. Renewable deficits are extracted from feeder time-series results in MW and converted to a common 10 MVA dynamic base before frequency simulation. For the IEEE 33-bus feeder, increasing renewable penetration from 0% to 100% keeps the minimum voltage close to 1.0 pu but raises the maximum voltage from 1.0295 pu to 1.0826 pu and increases feeder losses from 0.0246 MW to 0.1531 MW. The 24 h maximum voltage reaches 1.0755 pu at 100% penetration, whereas thermal loading remains

below its limit. For the corrected 75% severe event, the baseline nadir is 49.9695 Hz, droop support improves it to 49.9794 Hz, and droop plus FFR improves it to 49.9924 Hz. Under droop plus FFR, the severe-case nadir at 100% penetration is 49.9898 Hz. The 1 MW and 2 MW headroom cases are effectively identical because neither reaches saturation under the corrected disturbances. Overall, upper voltage is the earliest binding screening constraint from 50% penetration onward, while loading and supported frequency remain non-binding for the investigated cases. These conclusions are feeder-specific and planning-oriented; they do not replace EMT, protection, converter-current, or long-duration battery-energy studies. Future work should include higher-resolution renewable profiles, EMT and hardware-in-the-loop validation, explicit grid-strength sensitivity, state-of-charge and energy-duration constraints, Volt/VAR control, curtailment, and coordinated storage dispatch.

Author Contributions: Conceptualization, S.A.I.; methodology, S.A.I., O.A.A. and E.E.O.; software, S.A.I.; formal analysis, S.A.I.; investigation, S.A.I., O.A.A. and E.E.O.; resources, S.A.I., O.A.A. and E.E.O.; writing—original draft preparation, S.A.I.; writing—review and editing, S.A.I., O.A.A. and E.E.O.; supervision, O.A.A. and E.E.O.; funding acquisition, E.E.O. All authors have read and agreed to the published version of the manuscript.

Funding: This research received no external funding.

Data Availability Statement: The feeder data, OpenModelica files, PowerFactory and PSAT benchmark files, and Python automation scripts used in this study are available via GitHub: https://github.com/Directbookstore/Inertia-and-Frequency-Stability-Assessment-for-Renewable-Rich-Distribution-Feeders.git (accessed on 15 June 2026).

Conflicts of Interest: The authors declare no conflicts of interest.

References

1. Markovic, U.; Stanojev, O.; Aristidou, P.; Vrettos, E.; Callaway, D.; Hug, G. Understanding small-signal stability of low-inertia systems. *IEEE Trans. Power Syst.* **2021**, *36*, 3997–4017. [CrossRef]
2. Denholm, P.; Mai, T.; Kenyon, R.W.; Kroposki, B.; O'Malley, M. *Inertia and the Power Grid: A Guide Without the Spin*; National Renewable Energy Laboratory: Golden, CO, USA, 2020.
3. Baran, M.E.; Wu, F.F. Network reconfiguration in distribution systems for loss reduction and load balancing. *IEEE Trans. Power Deliv.* **1989**, *4*, 1401–1407. [CrossRef]
4. Seidaliseifabad, M.; Ma, J. Photovoltaic hosting capacity sensitivity to active distribution network management. *IEEE Trans. Power Syst.* **2021**, *36*, 107–117. [CrossRef]
5. He, C.; Geng, H.; Rajashekara, K.; Chandra, A. Analysis and control of frequency stability in low-inertia power systems: A review. *IEEE/CAA J. Autom. Sin.* **2024**, *11*, 2363–2383. [CrossRef]
6. Saleem, M.I.; Saha, S.; Roy, T.K. Inertia sensitivity analysis of power grids with high penetration of renewable energy sources. *IEEE Trans. Ind. Appl.* **2025**, *61*, 5362–5380. [CrossRef]
7. Hu, S.; Yang, J.; Wang, Y.; Zhao, Y.; Chao, C. Inertia and primary frequency response requirement assessment for high-penetration renewable power systems based on planning perspective. *Sustainability* **2023**, *15*, 16191. [CrossRef]
8. Lyu, X.; Groß, D. Grid forming fast frequency response for PMSG-based wind turbines. *IEEE Trans. Sustain. Energy* **2024**, *15*, 23–38. [CrossRef]
9. Meng, L.; Zafar, J.; Khadem, S.K.; Collinson, A.; Murchie, K.C.; Coffele, F.; Burt, G.M. Fast frequency response from energy storage systems—A review of grid standards, projects and technical issues. *IEEE Trans. Smart Grid* **2020**, *11*, 1566–1581. [CrossRef]
10. Zhang, J.; Wang, H.; Liu, G.; Tian, G.; Rivera, M.; Wheeler, P. Virtual synchronous generator control strategy of grid-forming matrix converter for renewable power generation. *IEEE Access* **2024**, *12*, 106672–106684. [CrossRef]
11. Khazaei, J.; Tu, Z.; Liu, W. Small-signal modeling and analysis of virtual inertia-based PV systems. *IEEE Trans. Energy Convers.* **2020**, *35*, 1129–1138. [CrossRef]
12. Aljarrah, R.; Fawaz, B.B.; Salem, Q.; Karimi, M.; Marzooghi, H.; Azizipanah-Abarghooee, R. Issues and challenges of grid-following converters interfacing renewable energy sources in low inertia systems: A review. *IEEE Access* **2024**, *12*, 5534–5561. [CrossRef]
13. Cui, H.; Konstantinopoulos, S.; Osipov, D.; Wang, J.; Li, F.; Tomsovic, K.L. Disturbance propagation in power grids with high converter penetration. *Proc. IEEE* **2023**, *111*, 873–890. [CrossRef]

14. Zhou, J.; Guo, Y.; Yang, L.; Shi, J.; Zhang, Y.; Li, Y.; Guo, Q.; Sun, H. A review on frequency management for low-inertia power systems: From inertia and fast frequency response perspectives. *Electr. Power Syst. Res.* **2024**, *228*, 110095. [CrossRef]
15. Shah, C.; Vasquez-Plaza, J.D.; Campo-Ossa, D.D.; Patarroyo-Montenegro, J.F.; Guruwacharya, N.; Bhujel, N.; Trevizan, R.D.; Rengifo, F.A.; Shirazi, M.; Tonkoski, R.; et al. Review of dynamic and transient modeling of power electronic converters for converter dominated power systems. *IEEE Access* **2021**, *9*, 82094–82117. [CrossRef]
16. Thurner, L.; Scheidler, A.; Schafer, F.; Menke, J.-H.; Dollichon, J.; Meier, F.; Meinecke, S.; Braun, M. pandapower—An open-source Python tool for convenient modeling, analysis, and optimization of electric power systems. *IEEE Trans. Power Syst.* **2018**, *33*, 6510–6521. [CrossRef]
17. Tests and Validation. Pandapower Documentation. Available online: https://www.pandapower.org/about/ (accessed on 7 April 2026).
18. Milano, F. An open source power system analysis toolbox. *IEEE Trans. Power Syst.* **2005**, *20*, 1199–1206. [CrossRef]
19. Kundur, P. *Power System Stability and Control*; McGraw-Hill: New York, NY, USA, 1994.
20. Nigerian Electricity Regulatory Commission. *The Grid Code for the Nigeria Electricity Transmission System*; Version 03; Nigerian Electricity Regulatory Commission: Abuja, Nigeria, 2018.
21. *IEEE Std 1547-2018*; IEEE Standard for Interconnection and Interoperability of Distributed Energy Resources with Associated Electric Power Systems Interfaces. IEEE: New York, NY, USA, 2018.
22. Tsili, M.; Papathanassiou, S. A review of grid code technical requirements for wind farms. *IET Renew. Power Gener.* **2009**, *3*, 308–332. [CrossRef]
23. Khan, B.; Guerrero, J.M.; Chaudhary, S.; Vasquez, J.C.; Frederiksen, K.H.B.; Wu, Y. A review of grid code requirements for the integration of renewable energy sources in Ethiopia. *Energies* **2022**, *15*, 5197. [CrossRef]
24. Nigerian Electricity Regulatory Commission. Distribution Code for the Nigerian Electricity Supply Industry, Version 02, Sec. 4.3.1, p. 33, 2019. Available online: https://nerc.gov.ng/wp-content/uploads/2018/07/Distribution%20Code_v02.pdf (accessed on 8 May 2026).
25. Mohammadpour, A.; Walinga, S. Megapack Grid-Forming: Enabling Simplicity and Flexibility in BESS Projects. In *Presented at ESIG*; Tesla Inc.: Austin, TX, USA, 2025.

Disclaimer/Publisher's Note: The statements, opinions and data contained in all publications are solely those of the individual author(s) and contributor(s) and not of MDPI and/or the editor(s). MDPI and/or the editor(s) disclaim responsibility for any injury to people or property resulting from any ideas, methods, instructions or products referred to in the content.